17th INTERNATIONAL FOUNDRYMEN CONFERENCE
Hi-tech casting solution and knowledge based engineering
Opatija, May 16th-18th, 2018

ANALYSIS OF THE LOW ENERGY LAYERING FRACTURE IN Al-2.5Mg-0.7Li ALLOY

Franjo Kozina[1], Zdenka Zovko Brodarac[1], Mitja Petrič[2]

[1]University of Zagreb Faculty of Metallurgy, Sisak, Croatia
[2]University of Ljubljana Faculty of Natural Science and Engineering, Ljubljana, Slovenia

Abstract

The mechanism of nucleation and propagation of low energy layering fracture, observed during thermo-mechanical testing of Al-2.5Mg-0.7Li alloy in as cast condition, was analyzed. Since the low energy layering fracture is affected by Li segregations and microstructural constituents' development, solidification sequence of Al-2.5Mg-0.7Li alloy was investigated in equilibrium and non-equilibrium conditions. Results of the investigations have shown that Mg has more pronounced effect on low energy layering fracture due to reducing solubility of Li in liquid phase and α_{Al}, maximizing precipitation of hardening (Al_3Li) δ' phase, ternary (Al_2LiMg) T phase and (Al_8Mg_5) β phase, and reducing ductility by solid solution hardening.

Keywords: *Al-Mg-Li alloy, phase precipitation, Li solubility, solidification sequence, low energy delamination fracture*

INTRODUCTION

Density reduction, stiffness increase [1], increase in fracture toughness [2], fatigue crack growth resistance [3] and crack propagation behavior [4] (nucleation and growth of small [5] and long [6] cracks) as well as enhanced corrosion resistance [7] are considered to be the benefits of aluminum-magnesium-lithium (Al-Mg-Li) alloy application. The mechanical properties of Al-Mg-Li alloys are the result of microstructural constituents' development during solidification and/or thermo-mechanical processing [8]. Microstructural constituents characteristic for Al-Mg-Li alloys are nature and volume fraction of strengthening precipitates [9], amount of coherent precipitates that alter the planar slip deformation behavior [10], content, size and distribution of coarse and angular equilibrium precipitates [9] as well as formation and widening of low precipitation frequency zone (PFZ) [1]. Microstructural constituents' developed during solidification are influenced by chemical composition, thermodynamic parameters and processing parameters.

Each weight percent of Li added decreases the density by approximately 3 % [11] and increases Young's modulus by 6 % [12], for the additions up to 4 wt. % [13]. However, maximum strength is obtained in the range of 1.1-1.3 wt.% Li [14]. Increasing of Li content above 1.3 wt.% will result in yield and tensile strength decrease, respectively [15]. Furthermore, according to [16, 17] alloys with Li content greater than 1 wt.% are prone to

low energy layering fracture. Layering fracture is characterized by the failure along the grain boundaries [18]. Low energy layering fracture is attributed to Li segregations at grain boundaries [18, 19], high frequency of grain boundary precipitates [20] followed by the formation of PFZ at the grain boundaries [21] and planar slip band formation [22]. The grain boundary segregation and non-uniformly distributed precipitates are result of coarse grain structure developed during solidification. Developed coarse grain structure has a preferred crystallographic orientation or texture with respect to ingot geometry. A preferred crystallographic orientation and evaluated texture cause anisotropy of mechanical properties [23]. Since the grain boundary area is small, high volume fraction of grain boundary precipitates form a continuous film. Formation of continuous film weakens grain boundaries enabling nucleation and propagation of cracks along the grain boundaries [20]. PFZ is formed during the reaction between grain boundary precipitates and pockets of bulk liquid. Widening of PFZ is a result of phase precipitation in the solid solution [24]. The low precipitation frequency increases plasticity and stress around grain boundary precipitates leading to the vacancy nucleation [25]. Additionally, the vacancy nucleation is facilitated by the planar slip bands impinging on the grain boundaries [26].

The solidification surface in the Al corner of the Al-Li-Mg system is given in Figure 1. The corresponding invariant reactions are given in Table 1.

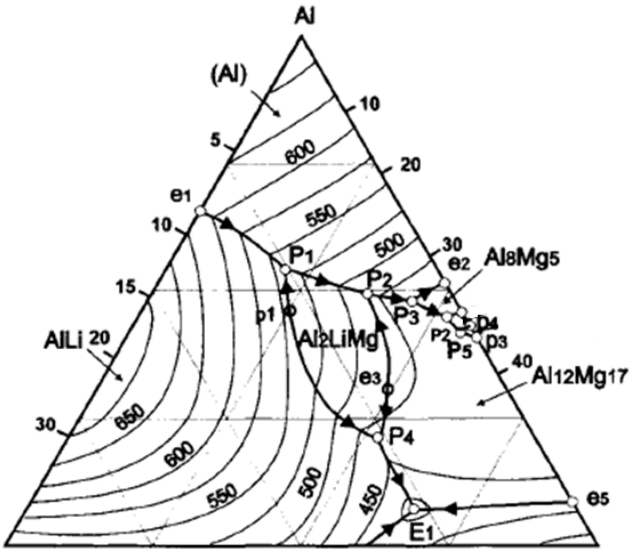

Figure 1. Liquids projection in the Al corner of Al-Li-Mg ternary phase diagram [27]

Table 1. Invariant equilibrium reactions in the Al corner of Al-Li-Mg phase diagram [27]

Point in Figure 1.	Reaction	Concentration in liquid phase, at. %		Temperature, °C
		Li	Mg	
e1	$L \rightarrow \alpha_{Al}+AlLi(\delta)$	7.5	-	602
P1	$L+AlLi \rightarrow \alpha_{Al}+Al_2LiMg(T)$	19.4	14.6	536
P2	$L+Al_2LiMg(T) \rightarrow \alpha_{Al}+Al_{12}Mg_{17}(\gamma)$[32]	10.8	27.7	483
P3	$L+\alpha_{Al}+Al_{12}Mg_{17} \rightarrow Al_8Mg_5(\beta)$	6.0	33.5	458
P4	$L+Al_2LiMg \rightarrow AlLi+ Al_{12}Mg_{17}$	20.1	40.1	464
e2	$L \rightarrow \alpha_{Al}+Al_8Mg_5(\beta)$	-	34	450

Based on the liquids projection in the Al corner following phases are in equilibrium with the α_{Al} solid solution: AlLi (δ), Al_2LiMg (T), $Al_{12}Mg_{17}$ (γ) and Al_8Mg_5 (β) (Figure 1). According to the Table 1., solidification begins with the eutectic reaction at 602°C involving primary α_{Al} dendrite network development and precipitation of stable δ phase (e1). Ternary T phase precipitates during peritectic reaction between stable δ phase and bulk liquid phase enriched in Mg (P1). T phase is the only ternary phase in this system existing in the range of 10.3 % to 11.3 % of Li and 27.1 % to 24.0 % of Mg respectively [28]. It has a complex cubic lattice and tends to precipitate at high angle grain boundaries [29]. Since stable δ phase is dissolved, precipitation of T phase leads to formation of PFZ. The low precipitation frequency areas have a low crack resistance and contribute to the formation of cracks at the grain boundaries. The creep and crack resistance is additionally reduced by precipitation of γ phase [30] (P3) and secondary eutectic β phases [31] (e2). The additions of Li narrow the composition range of β phase and widen homogeneity of γ [27] phase area. Consequently, γ phase stays in equilibrium with α_{Al} (P4) longer. The irregular coarse particles of β phase precipitate at the grain boundaries as a secondary eutectic phase [27].

The solid solubility of Li and Mg in α_{Al} related to temperatures is given in Figure 2. The mutual solid solubility of Li and Mg in α_{Al} at 470°C, 430°C and 200°C is indicated in Table 2.

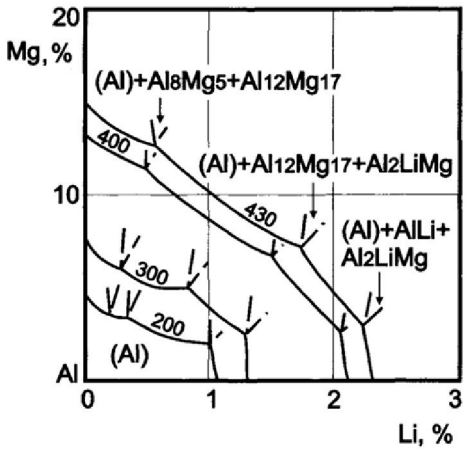

Figure 2. Solid solubility of Li and Mg in α_{Al} related to temperatures [33]

Table 2. Mutual solid solubility of Li and Mg in α_{Al} at different temperatures [27]

T, °C	$\alpha_{Al}+Al_{12}Mg_{17}+Al_8Mg_5$		$\alpha_{Al}+Al_{12}Mg_{17}+Al_2LiMg$		$\alpha_{Al}+AlLi+ Al_2LiMg$	
	Mg,%	Li, %	Mg,%	Li, %	Mg,%	Li, %
470	14.0	0.8	9.3	1.4	3.8	3.0
430	12.5	0.55	7.2	1.72	3.0	2.25
200	3.6	0.19	3.4	0.32	2.0	1.0

Mg reduces solubility of Li resulting in the formation of high volume fraction of Al-Li based precipitates, mainly δ and T phase [33]. Despite precipitation of γ and β phase, solid solution of α_{Al} stays enriched in Mg (Table 2). Consequently, Mg enrichment enhances lattice of α_{Al} causing solid solution strengthening [34].

Thermodynamic parameters, mainly cooling rate, significantly influence solidification sequence. Equilibrium solidification of 1420 alloy, containing 5.5 % Mg and 2.0 % Li, involves

only formation of α_{Al} dendrite network. The δ and T phase precipitate in solid state. However, in real, non-equilibrium conditions, solidification require transformation of α_{Al} dendrite network and eutectic precipitation of stable δ phase [35]. Ternary T phase precipitates during peritectic reaction between stable δ phase and liquid phase. Since stable δ phase is dissolved, precipitation of T phase causes formation of low precipitation frequency areas. Since Mg reduces solubility of Li in α_{Al} high volume fraction of δ and T phase is expected. By the end of solidification sequence, α_{Al} lattice stays enhanced due to the Mg enrichment [32].

Taking into account all interactions, the possible causes of low energy layering fracture represent a synergy of Li segregations at grain boundaries, high frequency of grain boundary precipitates, formation of PFZ at the grain boundaries and planar slip band formation. Layering fracture is unlikely caused by Li segregations because of its reduced solubility in liquid phase (Table 1, point e1, e2, P1, P4) and α_{Al} (Table 2). Since Mg significantly reduces solubility of Li in α_{Al}, Mg has more pronounced effect on microstructural constituents' development and mechanical properties.

The goal of this research is to understand mechanism of layering crack formation observed during thermo-mechanical testing of Al-2.5Mg-0.7Li alloy in as cast condition. Solidification sequence under equilibrium conditions was identified using Computer Aided Thermodynamic Diagram Calculation (CALPHAD). CALPHAD enabled tracking interactions of Li and Mg with bulk α_{Al} as well as solidification sequence prediction and reactions in both liquid and solid state respectively. Microstructural constituents development under non-equilibrium conditions was identified using differential scanning calorimetry (DSC), metallographic analysis and X-ray diffraction (XRD).

MATERIALS AND METHODS

The Al-2.5Mg-0.7Li alloy was synthesized in an induction melting furnace under protective atmosphere of argon (Ar) and crucible cover. The alloy was cast into a permanent steel mold without protective atmosphere. Chemical composition of synthesized alloy was determined using ARL™ 4460 Optical Mass Spectroscope.

Application of CALPHAD enabled identification of solidification sequence under equilibrium conditions. Significant temperatures of phase transformations and precipitations were determined using DSC method. The samples were tested using heating and cooling rates of 50, 10, 2 K/min. Comparison of significant temperatures of phase transformations and precipitations with results from XRD and metallographic analysis enabled determination of solidification in non-equilibrium conditions.

Samples for metallographic analysis were prepared using grinding/polishing machine Pheonix Beta Biller SAD. In order to observe grain boundaries and precipitates, samples were etched using Poulton's, Keller's and Weck's etching solutions. Macrostructure was observed using stereo microscope Olympus SZ11. The Olympus GX51 inverted metallographic microscope was used to perform light microscopy. Electron microscopy was done on Tescan, Vega TS 5136 MM equipped with energy dispersive spectrometer (EDS). Since EDS does not

have a possibility for Li identification, exact prediction of present phases was done by XRD method using Philips PANalyticalX'Pert PRO X-ray diffractometer.

Compression testing was conducted on GLEEBLE 1500 D machine. The sample in as cast condition was tested at room temperature. The force of 1.3 N was applied with strain rate of 230 mm/min.

RESULTS AND DISCUSSION

Phase transformation and precipitations under equilibrium conditions, determined using Thermo-Calc software support, are given in Figure 3.

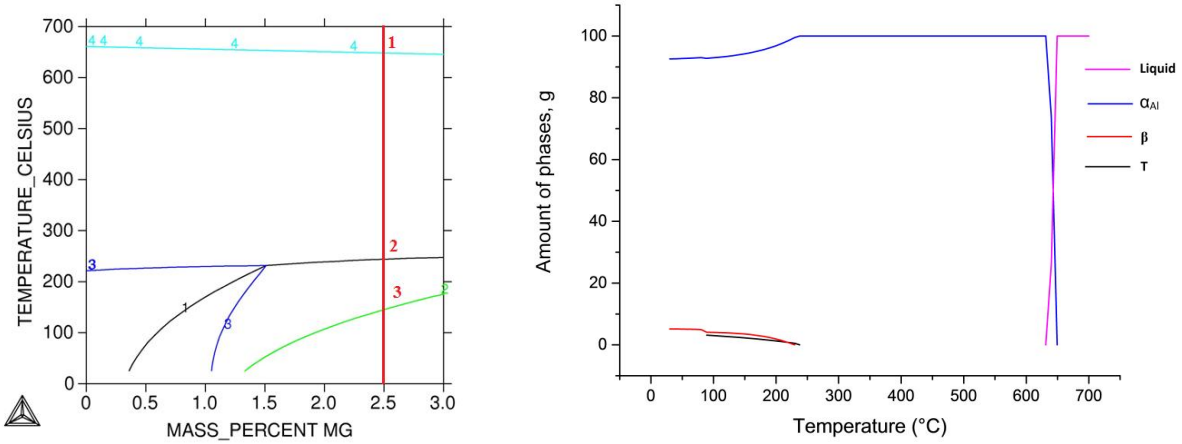

a) b)

Figure 3. The Al-rich corner of Al-Mg-Li ternary diagram:
a) Al-Li-Mg ternary phase diagram with respect to Mg,
b) Amount of phases developed during solidification

Solidification sequence according to the equilibrium phase diagram is given in Table 3.

Table 3. Solidification sequence according to Thermo-Calc calculations diagram in Figure 3 a

Reaction No.	Reaction	Temperature, °C
1	$L \rightarrow \alpha_{Al}$	640
2	$\alpha_{Al} \rightarrow \alpha_{Al}' + Al_2LiMg$ (T)	230
3	$\alpha_{Al}' \rightarrow \alpha_{Al}'' + Al_8Mg_5$ (β)	146.5

According to Thermo-Calc calculations, equilibrium solidification begins with transformation of α_{Al} dendritic network at 640°C (Figure 3 b). Ternary T phase and β phase precipitate in solid solution (Figure 3 a, b). The T phase precipitates at 230°C during eutectoid reaction followed by decrease in the amount of α_{Al} (Figure 3 b). Solidification sequence, under equilibrium conditions ends with the precipitation of β phase. The β phase precipitates from bulked α_{Al}' at 146.5°C.

The amount of components in liquid (L) phase is given in Figure 4.

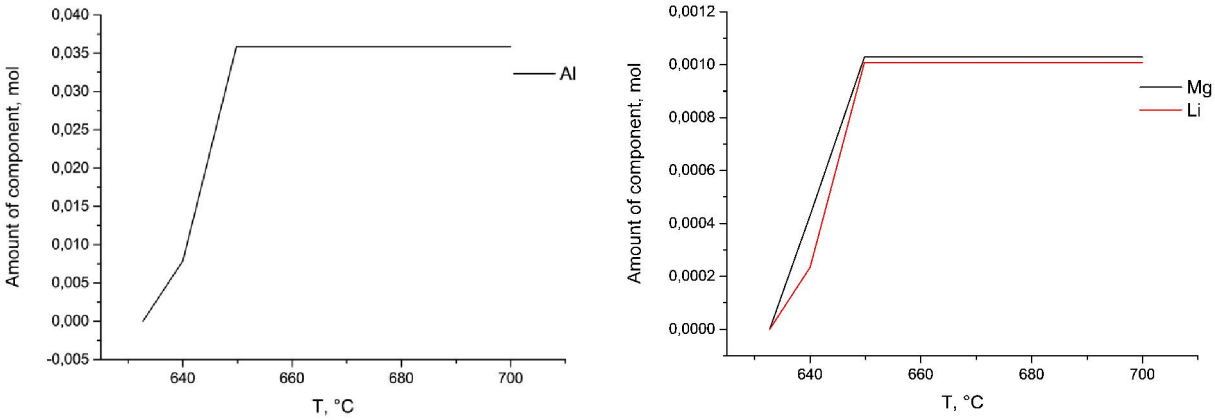

a) b)

Figure 4.Component ratio in L:
a) Al,
b) Mg and Li

The average content of Al in L phase (0.03588 mol) stays constant until the temperature of 640°C when it starts to drop rapidly. The rapid drop is caused by phase transformation resulting in dendritic network development (α_{Al}) (Figure 4 a). The changes in the amount of Mg (0.00103 mol) and Li (0.00101 mol) in L phase behave similarly (Figure 4 b).

The amount of components in α_{Al} is given in Figure 5 a and b.

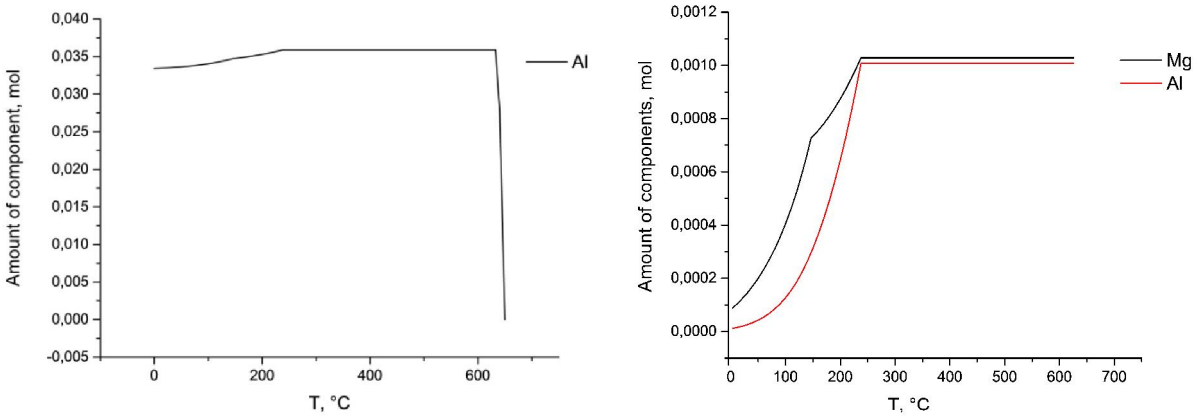

a) b)

Figure 5.Component ratio in α_{Al}:
a) Al,
b) Mg and Li

Based on the Figure 5 a, two changes in the average amount of Al (0.03588 mol) in α_{Al} can be found. The first drop in the average amount of Al is caused by eutectoid precipitation of ternary T phase at 230°C. The second drop in average amount of Al (0.037574 mol) is a result of precipitation of β phase at 146.5°C. At the end of solidification sequence, the average amount of Al in α_{Al} is 0.03341 mol. Starting average content of Mg is 0,00103 mol and Li is 0,00101 mol in $\alpha_{Al,}$ at 632.7°C respectively. The average amount of Li in α_{A} is rapidly reduced during the precipitation of ternary T phase because of the Mg influence and reduced

solubility. At the end of solidification the average content of Li in α_{Al} is $1.04706e^{-5}$ (Figure 5 b). During precipitation of ternary T phase at 230°C the average content of Mg in α_{Al} decreases to $9.93495e^{-4}$. However, the pronounced change in the amount of Mg in α_{Al} is caused by precipitation of β phase at 146.5°C (Figure 5 b). The average content of Mg in α_{Al}, at the end of solidification sequence is $8.30476e^{-5}$.

The amount of components in T phase is given in Figure 6 a and b.

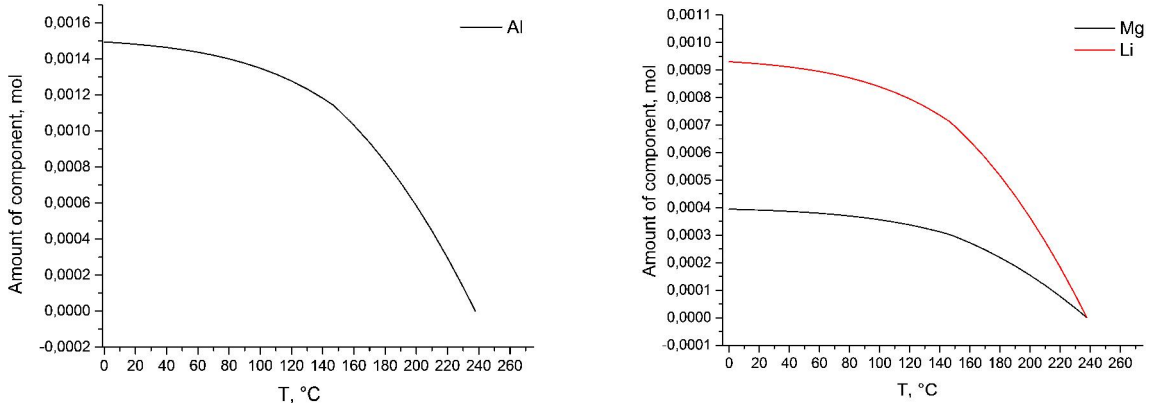

a) b)

Figure 6. Component ration in T phase:
a) Al,
b) Mg and Li

The average content of Al in ternary T phase grows from starting $1.32877e^{-4}$ mol at 230°C to 0.00149 mol at the end of solidification (Figure 6 a). Since Mg reduces solubility of Li in α_{Al}, the amount of Li in T phase grows exponentially from the starting $8.27349e^{-5}$ mol until the temperature of 146.5°C (Figure 6 b) and precipitation of β phase. The average content of Li at the end of solidification sequence is $9.3045e^{-4}$ mol. After precipitation of β phase begins at 146.5°C, the amount of Mg in ternary T phase grows slowly from starting $3.50997e^{-5}$ to $3.94737e^{-4}$ (Figure 6 b).

The amount of components in β phase is given in Figure 7 a and b.

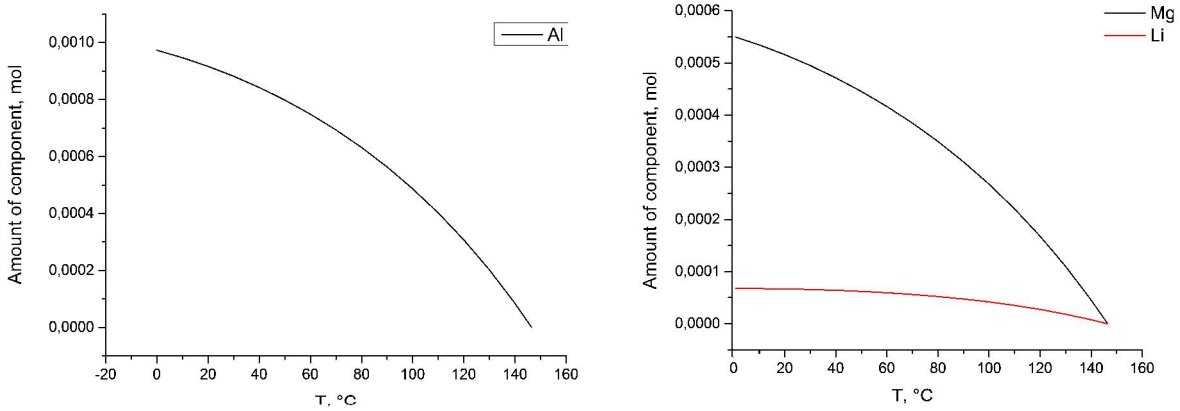

a) b)

Figure 7. Component ration in β phase:
a) Al,
b) Mg and Li

The starting average content of Al is $8.35005e^{-5}$ mol and Mg is $4.53609e^{-5}$ mol in β phase at 146.5°C respectively. At the end of solidification sequence, β phase contains in average $9.7274e^{-4}$ Al and $5.50811e^{-4}$ Mg. The average content of Li in β phase grows from starting $7.72156e^{-6}$ mol to $6.75787e^{-5}$ mol at the end of solidification sequence.

Calculation of Al-2.5Mg-0.7Li alloy under equilibrium conditions, involves only transformation of α_{Al} phase (Figure 5 a). Ternary T phase and β phase precipitate from the solid solution of α_{Al} phase (Figure 5 b). The reduced solubility of Li in α_{Al} phase causes precipitation of T phase leading to the significant depletion of Li from α_{Al} (Figure 5 b and Figure 6 b). Even due Mg is depleted from α_{Al} during precipitation of T phase, the amount of Mg is more significantly reduced during precipitation of β phase (Figure 5 b and Figure 6 b).

The influence of heating and cooling rates on the solidification sequence of Al-2.5Mg-0.7Li alloy is shown in Table 4.

Table 4. Influence of heating and cooling rate on solidification sequence

Heating rate, K/min			Cooling rate, K/min			Reaction
50	10	2	50	10	2	
659.9	666.0	651.0	639.7	643.1	643.8	$L \rightarrow \alpha_{Al}$
612.7	647.3	620.0	588.4	638.8	635.1	$L + \alpha_{Al} \rightarrow \alpha_{Al} + Al_3Li$ (δ')
--	608.1	605.8	540.8	594.2	617.8	$\alpha_{Al} + \delta' \rightarrow \alpha_{Al}' + \delta$
--	356.8	492.5	--	--	546.1	$\alpha_{Al}' + \delta' \rightarrow \alpha_{Al}'' + T$
--	313.8	368.5	--	--	--	$\alpha_{Al}'' \rightarrow \alpha_{Al}''' + \beta$

Solidification sequence of Al-2.5Mg-0.7Li alloy under non-equilibrium conditions begins with transformation of α_{Al}. Reduced solubility of Li in remaining L phase, and already formed α_{Al} leads to eutectic reaction resulting with precipitation of metastable δ' inside the α_{Al} grains. Precipitation of δ' is aided by constitutional undercooling due to the Mg influence. With further temperature decrease, stable δ phase nucleates on the grain boundaries of α_{Al}. Stable δ phase evaluated by reaction of previously precipitated α_{Al} and metastable δ' phase. Dissolution of δ' phase causes formation of PFZ near the grain boundaries. Elongated ternary phase precipitates due to the reaction of Mg from bulk α_{Al}' and already precipitated δ' phase. Precipitation of T phase leads to the further reduction of precipitation frequency. Solidification sequence ends with precipitation of secondary eutectic β phase followed by decrease in Mg content of α_{Al}''.

The microstructure of Al-2.5Mg-0.7Li is given in Figure 8. The individual phases were identified using literature survey comparison.

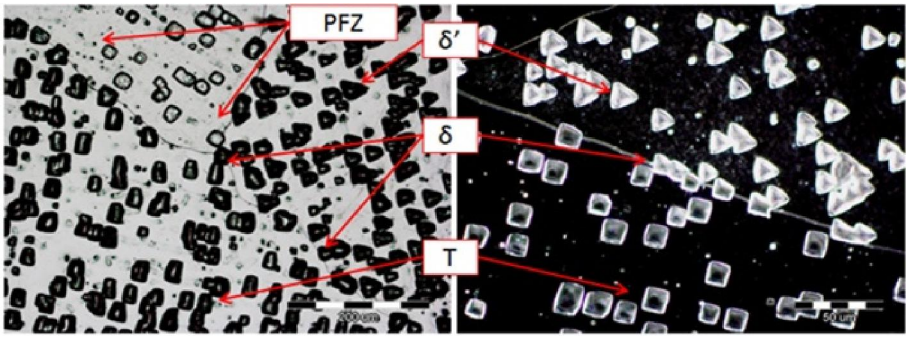

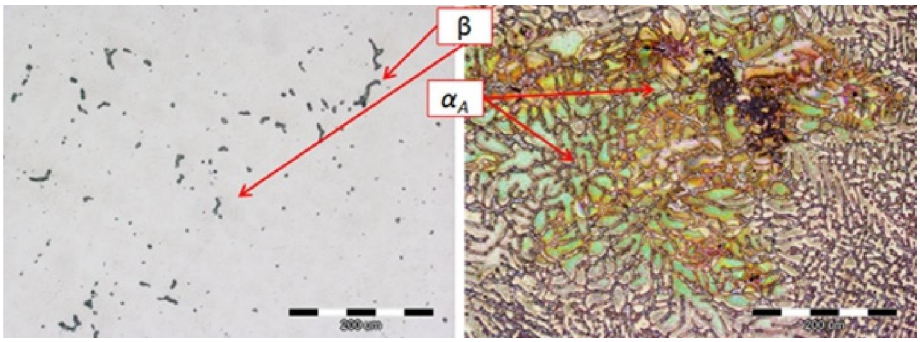

Figure 8. Microstructure of Al-2.5Mg-0.7Li

Particles of metastable δ' are found inside the grains of α_{Al} (Figure 8). The metastable δ' phase is a main strengthening precipitate in Al-Mg-Li alloys. It interacts with dislocations and leads to the formation of microstructural texture [11]. Stable δ phase can be found on grain boundaries. Precipitation of stable δ phase caused formation of PFZ near the grain boundaries (Figure 8). Ternary T phase can be found on the grain boundaries as well as inside the grains. Precipitation of T phase led to the further decrease of precipitation frequency (Figure 8) near the grain boundaries. Irregular coarse particles of secondary eutectic β phase can be found in the last solidifying areas (Figure 8).

The scanning electron image (SEI) and following mapping analysis are given in Figure 9 a and b. The positions for EDS quantitative analysis are indicated in Figure 9 a. The EDS is performed on characteristics phases at grain boundary as well as on different distances from it.

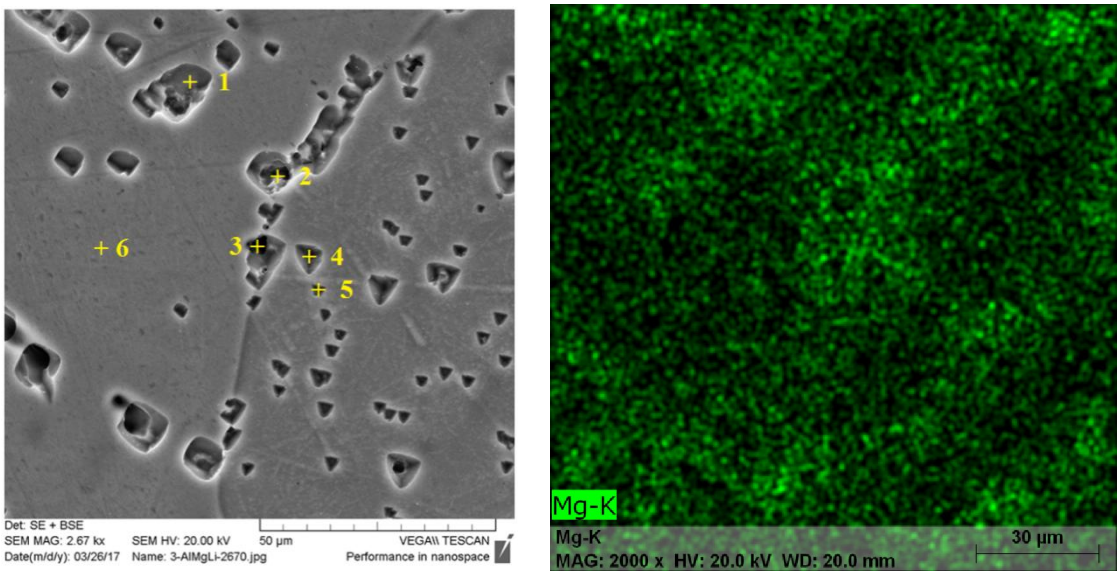

a) b)

Figure 9. SEI of:
a) Al-2.5Mg-0.7Li alloy with marked EDS analysis points
b) Mapping analysis of Mg content

Figure 9 a shows SEI of densely distributed phases in α_{Al} matrix. Results of mapping analysis show significant variations in color intensity concerning Mg content (Figure 9 b). Based on

the mapping analysis, highest concentration of Mg can be found near grain boundaries. Results of additional EDS quantitative analysis are given in Table 5.

Table 5. Results of EDS quantitative analysis

Location	Al, wt.%	Mg, wt.%
1	94.59	5.41
2	94.11	5.89
3	39.79	6.21
4	95.01	4.99
5	97.54	2.46
6	97.59	2.41

Since the measurements taken at the position 1-5 indicate the occurrence of different phases, measurements taken at the position 6 confirm the existence of residual Mg in bulk α_{Al}''.

Macrostructure of the sample's perpendicular quarter-section before compression testing is given in Figure 10 a. Microstructure of the sample in as cast condition is given in Figure 10 b.

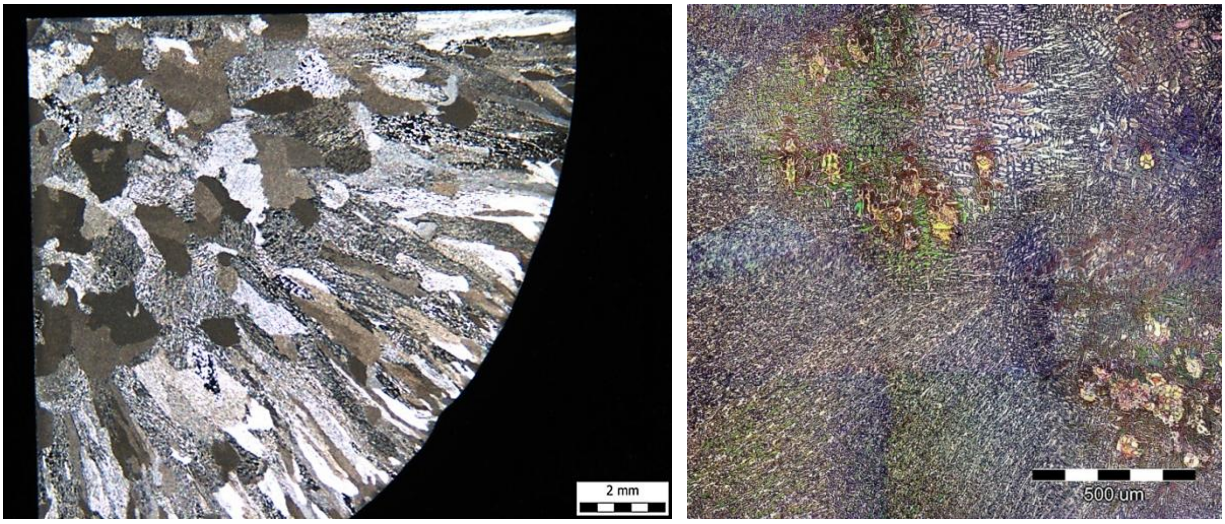

a) b)

Figure 10. Sample's quarter section perpendicular to the testing direction:
a) Macrostructure of the sample in as cast condition,
b) Microstructure of sample before compression testing, Multiple Image Alignment (MIA)

Sample exhibits typical structure for permanent mold castings. Formation of thin chill zone is followed by formation of columnar grains zone. Coarse equiaxed grains can be found in the middle of the sample (Figure 10 a).

Dendrites of α_{Al} developing in columnar zone have preferred orientation (Figure 10 b). The α_{Al} dendrites developing in equiaxed zone are coarse and filamentary (Figure 10 b).

Macrostructure of the sample after compression testing is given in Figure 11.

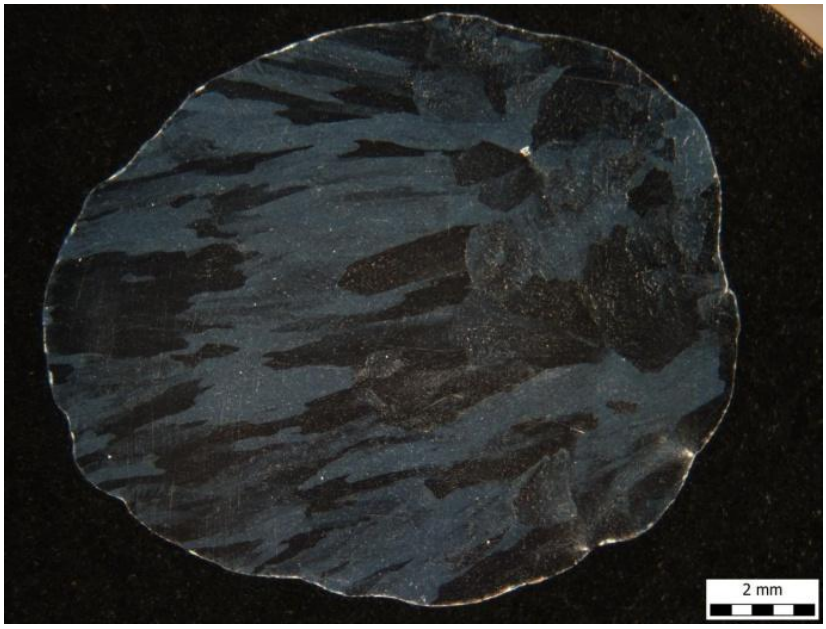

a)

b)

Figure 11.Macrostructure of the sample after compression testing:
a) Surface perpendicular to the testing direction,
b) Surface along the testing direction

The compression testing led to the significant texture development, as shown in Figure 11 a. Macrostructure of the surface parallel to the testing direction reveals significant cracking (Figure 11 b). The crack nucleated at the surface of the sample and propagated towards the center.

MIA of the area of the defects is given in Figure 12.

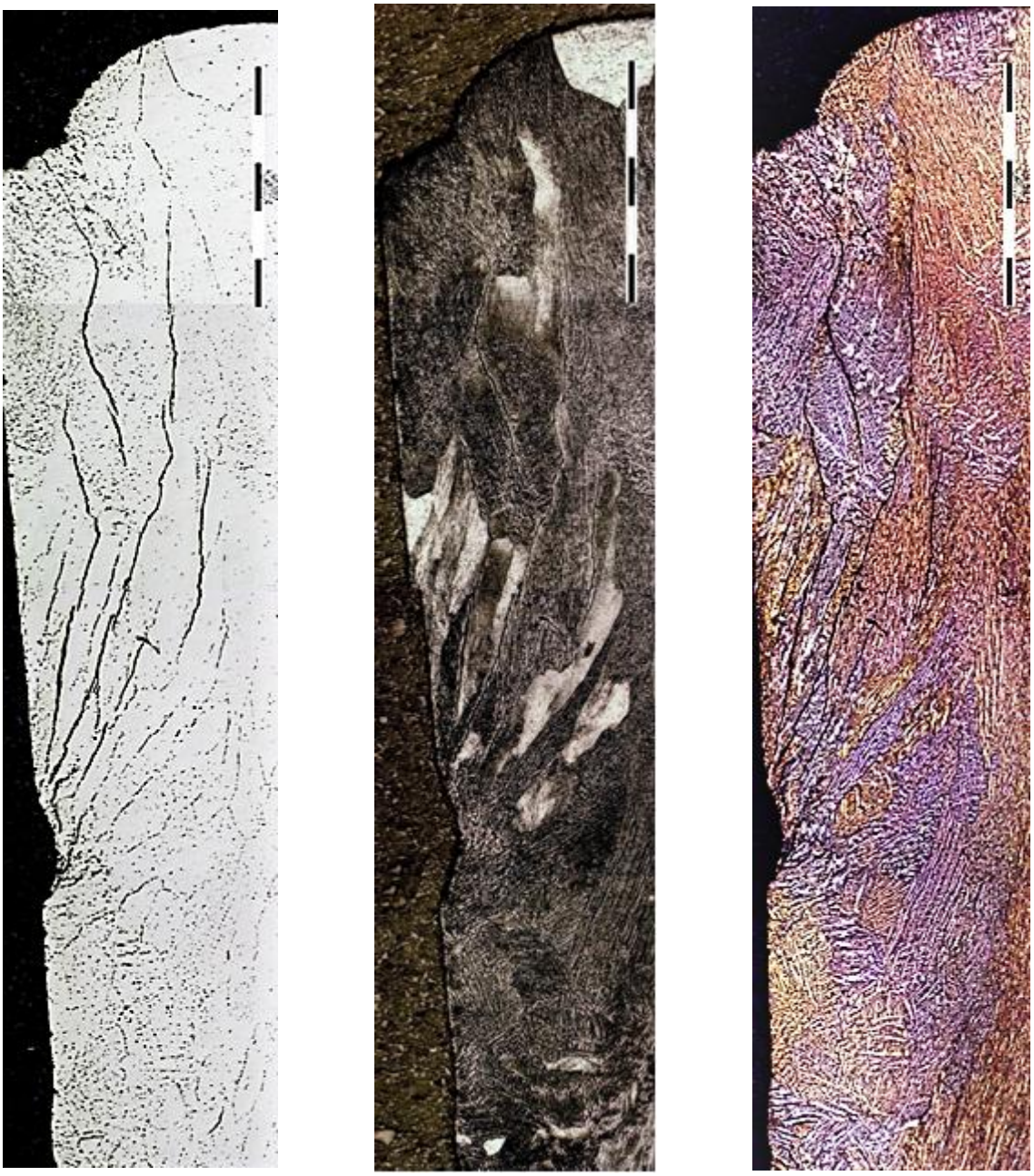

a) b) c)

Figure 12. MIA of the affected area in: a) As polished condition,
b) After etching with Poulton's etching solution,
c) After etching with Wecks's etching solution

The cracks nucleate at the surface defect and propagate towards the center of the sample, as shown in Figure 12 a. Etching to reveal the grain structure enabled identification of the defect as a failure along the grain boundaries (Figure 12 b). Result of color etching, given in Figure 12 c, indicated significant texture development in the area of the interest.

CONCLUSIONS

The mechanism of nucleation and propagation of low energy layering fracture, observed during thermo-mechanical testing of Al-2.5Mg-0.7Li alloy in as cast condition, was analyzed. Low energy layering fracture is influenced by Li segregations and microstructural constituents' development. Both, changes in the amount of components (Al, Li and Mg) in individual phases and solidification sequence of Al-2.5Mg-0.7Li alloy were investigated in equilibrium and non-equilibrium conditions.

Solidification sequence in equilibrium conditions involves transformation of α_{Al} followed by the precipitation of ternary T phase and β phase. The amount of Li in α_A is rapidly reduced during the precipitation of ternary T phase due to the reduced solubility and Mg influence.

Changes in solidification sequence under non-equilibrium conditions are a result of reduced solubility of Li in L phase and α_{Al}. Solidification sequence begins with transformation of α_{Al} dendritic network. Reduced solubility of Li in remaining L phase and α_{Al} leads to precipitation of metastable δ' inside the grains of α_{Al}. With temperature decrease, stable δ phase nucleates at the grain boundaries of α_{Al}. Stable δ phase grows on the account of previously precipitated α_{Al} and metastable δ' phase and leads to formation of PFZ near the grain boundaries. Precipitation of T phase widens the PFZ. Solidification sequence ends with precipitation of β phase at the grain boundaries.

Metallographic analysis of the sample, after compression testing, revealed low energy layering fracture as a failure along the grain boundaries. Interaction between δ' phase and dislocations caused textured development in the affected area. Precipitation of δ and β phase weakens the grain boundaries. Segregations of Mg at the grain boundaries led to the solid solution strengthening and ductility decrease.

The conducted investigations indicated that Mg has more pronounced effect on low energy delamination fracture development by:

- Reducing solubility of Li in L phase and α_{Al},
- Maximizing precipitation of hardening δ' phase particle,
- Precipitation of ternary T phase and widening PFZ,
- Precipitation of irregular β phase particles at the grain boundaries.
- Solid solution hardening.

REFERENCES

[1] R.J. Rioja, J. Liu, The evolution of Al-Li based products for aerospace and space applications, Metallurgical and Materials Transactions A, 43(2012)9, pp. 3325-3337.

[2] D. Tsivoulas, P. B. Prangnell, The effect of Mn and Zr dispersoid-forming additions on recrystalization in Al-Cu-Li AA2198 sheet, Acta Materialia, 77(2014)1, pp. 1-16.

[3] E. M. Rodrigues, A. Matias, L. B. Godefroid, F. L. Bastian, K. S. Al-Rubaie, Fatigue crack growth resistance and crack closure behavior in two aluminum alloys for aeronautical applications, Materials Research, 8(2005)3, pp. 287-291.
[4] K. V. Jata, E. A. Starke, Fatigue crack growth and fracture toughness behavior of an Al-Li-Cu alloy, Metallurgical Transactions A, 17(1986)6, pp. 1011-1026.
[5] R. K. T. Venkateswara, W. You, R. O. Ritchie, Fatigue crack propagation in aluminum-lithium alloys 2090: Part II. Small crack behavior, Metallurgical Transactions A, 19(1988)3, pp. 563-569.
[6] R. K. T. Venkateswara, W. You, R. O. Ritchie, Fatigue crack propagation in aluminum-lithium alloys 2090: Part I. Long crack behavior, Metallurgical Transactions A, 19(1988)3, pp. 549-561.
[7] K. I. Moore, J. M. Sykes, S. C. Hogg, P. S. Grant, Pitting corrosion of Spray Formed Al-Li-Mg alloys, Corrosion Science, 50(2008)11, pp. 3221-3226.
[8] Z. W. Wang, P. B. Prangnell, Microstructure refinement and mechanical properties of severely deformed Al-Mg-Li alloys, Material Science and Engineering, A 328(2002)1-2, pp. 87-97.
[9] N. A. Belov, D. G. Eskin, A. A. Aksenov, Multicomponent phase diagrams: Application for commercial aluminum alloys, Elsevier Science, 2005.
[10] A. A. Csontos, E. A. Starke, The effect of inhomogeneous plastic deformation on the ductility and fracture behavior of age hardenable aluminum alloys, International Journal of Plasticity, 21(2005)6, 1097-1118.
[11] N. E. Prasad, A. A. Gokhale, P. R. Rao, Mechanical behavior of aluminum-lithium alloys, Sadhana, 28(2003)1-1, pp. 209-246.
[12] R. J. Rioja, Fabrication methods to manufacturing isotropic Al-Li alloys and products for space and aerospace applications, Material Science and Engineering, A 257(1998)1, pp. 100-107.
[13] R. K. Gupta, N. Nayan, G. Nagasireesha, S. C. Sherman, Development and characterization of Al-Li alloys, Material Science and Engineering, A 420 (2006)1-2, pp. 228-243.
[14] K. K. Sankaran, N. J. Grant, The structure and properties of splat-quenched aluminum alloy 2024 containing lithium additions, Material Science and Engineering, A 44(1980)2, pp. 213-227.
[15] T. Dursun, C. Soutis, Recent developments in advanced aircraft aluminum alloys, Materials and Design, 50(2014)1, pp. 862-871.
[16] A. Bois-Brochu, F. A. T. Goma, C. Blais, D. Larouche, R. Gauvin, J. Boselli, Al-Li alloy 2099-T83 Extrusions: Static Mechanical Properties, Microstructure and Texture, Advanced Material Research, 409(2011), pp. 29-34.
[17] H. Babel, J. Gibson, M. Tarkanian, C. Parrish, M. Prietto, A. Ordonez-Chu, H. Haberl, R. Clark, J. Ogren, O. S. Es Said, 2099 Aluminum-lithium with key-locked inserts for aerospace applications, Journal of Materials Engineering and Performance, 16(2007)5, pp. 584-591.
[18] S. P. Lynch, B. C. Muddle, T. Pasang, Ductile - to – brittle fracture transition in 8090 Al-Li alloys, Acta Materialia, 49(2001)15, pp. 2863-2874.
[19] S. P. Lynch, Fracture of 8090 Al-Li plate I. Short transverse fracture toughness, 136(1991), pp. 25-43.
[20] C. Schlesier, E. Nembach, Strengthening of aluminum-lithium alloys by long-range ordered δ'-precipitates, Acta Metallurgica et Materialia, 43(1995)11, pp. 3983-3990.

[21] S. Suresh, A. K. Vasudevan, M. Tosten, P. R, Howell, Microscopic and macroscopic aspects of fracture in lithium-containing aluminum alloys, Acta Materialia, 35(1987)1, pp. 25-46.
[22] H. Garmastani, S. R. Kalidindi, L. Williams, C. M. Bacaltchuk, C. Fountain, E. W. Lee, O. S. Es-Said, Modeling the evolution of anisotropy in Al-Li alloys: application to Al-Li 2090-T8-E41, International Journal of Plasticity, 18(2002)10, pp. 1373-1393.
[23] J. E. Gruzleski, Microstructure development during metalcasting, American Foundrymen's Society, Illinois, 2000.
[24] J. Augustyn-Pieniažek, H. Adrian, S. Rzadkosz, M. Choroszynski, Structure and mechanical properties of Al-Li alloys as cast, Archives of Foundry Engineering, 13(2013)2, pp. 5-10.
[25] A. Williamd, Microstructural analysis of aluminium alloy 2093 as a function of heat treatment, School of Metallurgy and Materials, The University of Birmingham, 2010.
[26]H. J. McQueen, Mechanisms in creep and hot working to high strain; microstructural evidence, inconsistencies. Part I: substructure evolution; grain interactions, Metallurgical Science and Technology, 28(2010)1, pp. 12-21.
[27] B. Dubost, P. Bombard, I Ansara, Experimental study and thermodynamic calculations of Al-Li-Mg equilibrium phase diagram, Journal de Physique Colloques, 48(1987)3, 473-479.
[28] L. F. Mondolfo, Aluminum alloys: Structure and properties, Elsevier, Amsterdam, 2013.
[29] A. Mogucheva, R. Kaibyshev, Microstructure and mechanical properties of an Al-Li-Mg-Sc-Zr alloy subjected to ECAP, Metals, 254(2016)6, pp. 1-14.
[30] H. Zang, S. L. Shang, Y. Wang, A. Saengdeejing, L. Q. Chen, Z. K. Liu, First-principles calculations of the elastic, phonon and thermodynamic properties of $Al_{12}Mg_{17}$, Acta Materialia, 58(2010)11, pp. 4012-4018.
[31] Z. Z. Brodarac, F. Unkic, J. Medved, P. Mrvar, Determination of solidification sequence of the AlMg9 alloy, Kovove Materialy-Metallic Materials, 50(2012)1, pp. 59-67.
[32] Materials Science International Team (MSIT), Light metal ternary system: Phase diagrams, crystallographic and thermodynamic data, Springer-Verlag, Berlin Heidelberg, 2005.
[33] N. Prasad, A. Eswara, A. Gokhale, R. J. H. Wanhill, Aluminium–lithium alloys, Aerospace Materials and Material Technologies, Butterworth-Heinemann, Oxford, 2013.
[34] S. Betsofen, M. Chizhikov, Quantitative Phase Analysis of Al-Mg-Li and Al-Cu-Li Alloys, Aluminium Alloys, 794(2014)1, pp. 915-920.
[35] W. J. Poole, M. A. Walls, D. J. Lloyd, Crystal analysis of nonequilibrium δ_{non}-phase in Al-Li-Mg alloys, Materials Science Forum, 519-521(2006), pp. 259-264.

Acknowledgements

This investigation has been performed in the frame of financial support for investigation of University of Zagreb: "Design and characterization of innovative engineering alloys" (TP167) and support of scientific research projects within the joint Croatian-Slovenian collaboration "Design and characterization of innovative aluminium – magnesium – lithium alloy" (2018-2019) financed by Ministry of Science and Education, Republic of Croatia.